Continental Fragments in the South China Block: Constraints From Crustal Radial Anisotropy

Tingzi Li[1,2], Mingming Jiang[3], Liang Zhao[1], Yang Chu[1], Weihua Yao[4], Bo Wan[1], Ling Chen[1], Yinshuang Ai[3], Thomas Bodin[5], and Huaiyu Yuan[2,6,7]

[1]State Key Laboratory of Lithospheric Evolution, Institute of Geology and Geophysics, Chinese Academy of Sciences, Beijing, China, [2]Centre for Exploration Targeting, University of Western Australia, Crawley, WA, Australia, [3]Key Laboratory of Earth and Planetary Physics, Institute of Geology and Geophysics, Chinese Academy of Sciences, Beijing, China, [4]Guangdong Provincial Key Lab of Geodynamics and Geohazards, School of Earth Sciences and Engineering, Sun Yat-sen University, Guangzhou, China, [5]Université Lyon 1, ENS de Lyon, CNRS, Lyon, France, [6]Geological Survey of Western Australia, Perth, WA, Australia, [7]Department of Natural Resources, Macquarie University, North Ryde, NSW, Australia

Abstract The lithospheric architecture of the South China Block (SCB) is crucial to understanding the formation and evolution of this distinctive and highly reworked continental lithosphere with over 3 billion years of tectonic history. However, due to a lack of high-resolution geophysical datasets, a detailed picture of the SCB lithosphere is absent, and fundamental questions regarding its formation, assembly, and subsequent reworking processes are actively debated. Assuming that unique deformation patterns due to such tectonic processes can be mapped by seismic anisotropy, we present a new crustal radially anisotropic shear-wave velocity model along a 1500-km seismic transect that spans the major tectonic domains of the SCB to characterize the past deformation processes. The new seismic models show significant lateral variations in seismic anisotropy and velocity, suggesting that the SCB consists of several separated (micro)continental blocks or terranes that likely have different origins and have survived the prolonged deformation history since the early formation of these continental fragments. Combining available geophysical datasets, we link individual crustal domains of distinct anisotropy to constrain the multiphase deformation processes of the SCB, including the early formation of the Proto-Yangtze and Cathaysia Blocks, the assembly of the SCB, and the subsequent reactivation of the interior and extensive deformation that have formed the Basin-and-Range style tectonics in the Cathaysia Block. We suggest that relict continental fragments have played critical roles in the formation and reactivation of the SCB lithosphere.

Plain Language Summary The South China Block (SCB) is a significant landmass in eastern Eurasia with a history of over 3 billion years of tectonic activities. Despite its stable continent-like appearance inferred from surface GPS measurements and scarce seismicity, the SCB exhibits a dichotomous path in its tectonic history, in which the Yangtze and Cathaysia Blocks evolved into a stable craton and a part of the continent that may have lost its root, respectively. This complex tectonic evolution is not well understood due to a lack of detailed information about the SCB's lithospheric structure. To address this, a dense seismic dataset was used to create a new radially anisotropic shear-wave velocity model of the SCB's shallow lithosphere. This model helps to characterize past and current deformation processes by linking unique deformation fabrics to seismic anisotropy. The results reveal that the SCB consists of multiple blocks with distinct seismic properties. Combining with other geophysical and geological data, the new seismic information pieces together a better understanding of how the SCB formed and evolved over time. We conclude that these small pieces or fragmented crust of the SCB played a critical role in the assembly and reworking of the landmass.

1. Introduction

The South China Block (SCB; Figure 1) has a long and complex history of crustal formation and evolution, as evidenced by crustal samples that span over 3.0 billion years ranging from 3.2 to 2.8 billion years in age in the Kongling Complex of the Yangtze Block (YB), to the ~80 million year old granitic magmatism in the Cathaysia Block (CaB; Zhao & Cawood, 2012; Wang et al., 2013). Despite the apparent stable continent appearance of the SCB from surface, for example, uniform GPS measurements and low seismicity (Wang & Shen, 2020), its tectonic history reveals two distinct paths, in which the internal Yangtze and Cathaysia Blocks have undergone divergent evolution—the former stabilizing as a craton while the latter experiencing partial root loss (e.g., Zhang

Writing – original draft: Tingzi Li
Writing – review & editing: Tingzi Li, Mingming Jiang, Liang Zhao, Yang Chu, Weihua Yao, Bo Wan, Ling Chen, Yinshuang Ai, Thomas Bodin, Huaiyu Yuan

et al., 2013). However, understanding this complex tectonic evolution is obscured by thick sedimentary deposits, strong fault deformation, and extensive magmatism resulting from the region's complex deformation processes. One crucial aspect in understanding the SCB's tectonic evolution lies in its early crust. Although Archean and Paleoproterozoic basement is widespread across the SCB (Zhang et al., 2013), age and compositional heterogeneities suggest multiple crustal blocks (or terranes) with distinct origins prior to the formation of the unified SCB through the Jiangnan Orogeny (Cawood et al., 2020). Yet, the nature and architecture of this multi-block crust, and the roles that the individual terranes played in the SCB's assembly and subsequent deformation processes remain unknown.

To target this problem, we aim at the shallow lithospheric architecture of the SCB by using seismic radial anisotropy. Seismic anisotropy describes the dependence of seismic wave speeds with respect to wave propagation direction (e.g., Park & Levin, 2002). In continental crust, seismic anisotropy is mainly caused by the shape-preferred orientation (SPO) of aligned cracks, melt lenses, faults or folds and similar structures with strong foliation/lamination, and crystallographic preferred orientation (CPO) of crustal anisotropic minerals (Almqvist & Mainprice, 2017; Mainprice & Nicolas, 1989; Weiss et al., 1999). In the upper crust, SPO-induced anisotropy is most prevalent, due to cracks and fine layering in response to local stress fields, while in the mid-to lower crust, anisotropic rocks, mainly mica and amphibole-rich, deform under strain to form CPO-induced anisotropy (Almqvist & Mainprice, 2017). Due to these links to composition and spatial distribution of crustal rocks, seismic anisotropy is often used to explore rock textures produced in past and current deformation processes (Park & Levin, 2002; Silver, 1996).

Radial anisotropy, alternatively termed as transverse isotropy according to Anderson (1961), pertains to the discrepancy in velocities of shear waves polarized horizontally (V_{sh}) and vertically (V_{sv}). Positive or negative radial anisotropic signals refer to higher shear-wave velocities in horizontal and vertical directions, respectively, and therefore provide insight into the lateral flow, deformation and layering of the crust or mantle (Almqvist & Mainprice, 2017; Park & Levin, 2002). For example, the large positive radial anisotropy observed in intermediate-period Rayleigh and Love waves propagating across Tibet is attributed to CPO-induced anisotropy formed by channelized crustal flow during the collision between India and Eurasia (Shapiro et al., 2004). Similarly, studies in the Western US have linked strong positive deep crustal anisotropy to the CPO of anisotropic crustal minerals in response to ductile deformation during the widespread extension of the Basin and Range province (Moschetti et al., 2010). Positive radial anisotropy has also been observed in the ductile mid-to lower crust, for example, in the Alps (Alder et al., 2021), eastern Tibet and surrounding areas (Huang et al., 2010; Li, Zhang, et al., 2021; Liu et al., 2021; Xie et al., 2013), the Eastern Himalayan Syntaxis (Hu et al., 2020), the North China Craton (Cheng et al., 2013; Fu et al., 2016), and South Africa (Malory et al., 2022). Conversely, negative radial anisotropy is often attributed to steeply dipping fractures or faults and/or large brittle deformation at the upper crust (Xie et al., 2017); crustal magma intrusion in a tilted fault interface (Luo et al., 2013), and mantle upwelling into the crust (Hu et al., 2020).

In this study, a new crustal radial anisotropic shear wave velocity (V_s) model is presented. We use the waveform data from an over 1,500-km long dense profile—South China Interior Structure Project 1 (SCISP-1; Figure 1)—and apply a cutting-edge transdimensional inversion technique that simultaneously inverts for isotropic V_s, radial anisotropy, and layer thickness. This study builds upon our previous work, which focused on the Proterozoic collision of South China (Li et al., 2022; see Section 2). The radial anisotropy results obtained here offer unique insights into the deformation history of the crustal rocks. As a result, this new approach presents a novel way to investigate the composition and roles of individual blocks within the multi-block crust of the SCB, shedding light on the assembly and subsequent deformation processes of continental lithosphere in general.

2. Tectonic Setting and Previous Crustal Studies

The SCB is comprised of the Yangtze and Cathaysia blocks, which converged along the Jiangnan Orogen during the Neoproterozoic period (e.g., Cawood et al., 2018). The overall age of rock units within the Yangtze and Cathaysia blocks ranges mostly from Mesoproterozoic to Paleoproterozoic time, indicating the SCB could have been assembled from a series of spatially unrelated domains (Cawood et al., 2020). The Yangtze basement further includes Archean to Paleoproterozoic rocks (i.e., Kongling, Kangding, Sibao, and Banxi), later outcropped by Neoproterozoic igneous and sedimentary rocks (Zhang et al., 2013). Within the Cathaysia Block there are several proposed fragments of the Shuangxiwu, Wuyi, Yunkai, and Coastal domains from west to east Cathaysia (Lin et al., 2018; Wang et al., 2014) based on geochemistry and geochronology constraints. Since the Neoproterozoic assembly, the SCB went through multi-stage intracontinental and intraplate tectonism to form its present tectonic framework, including the intracontinental orogenic and granitic magmatic events in the early Paleozoic
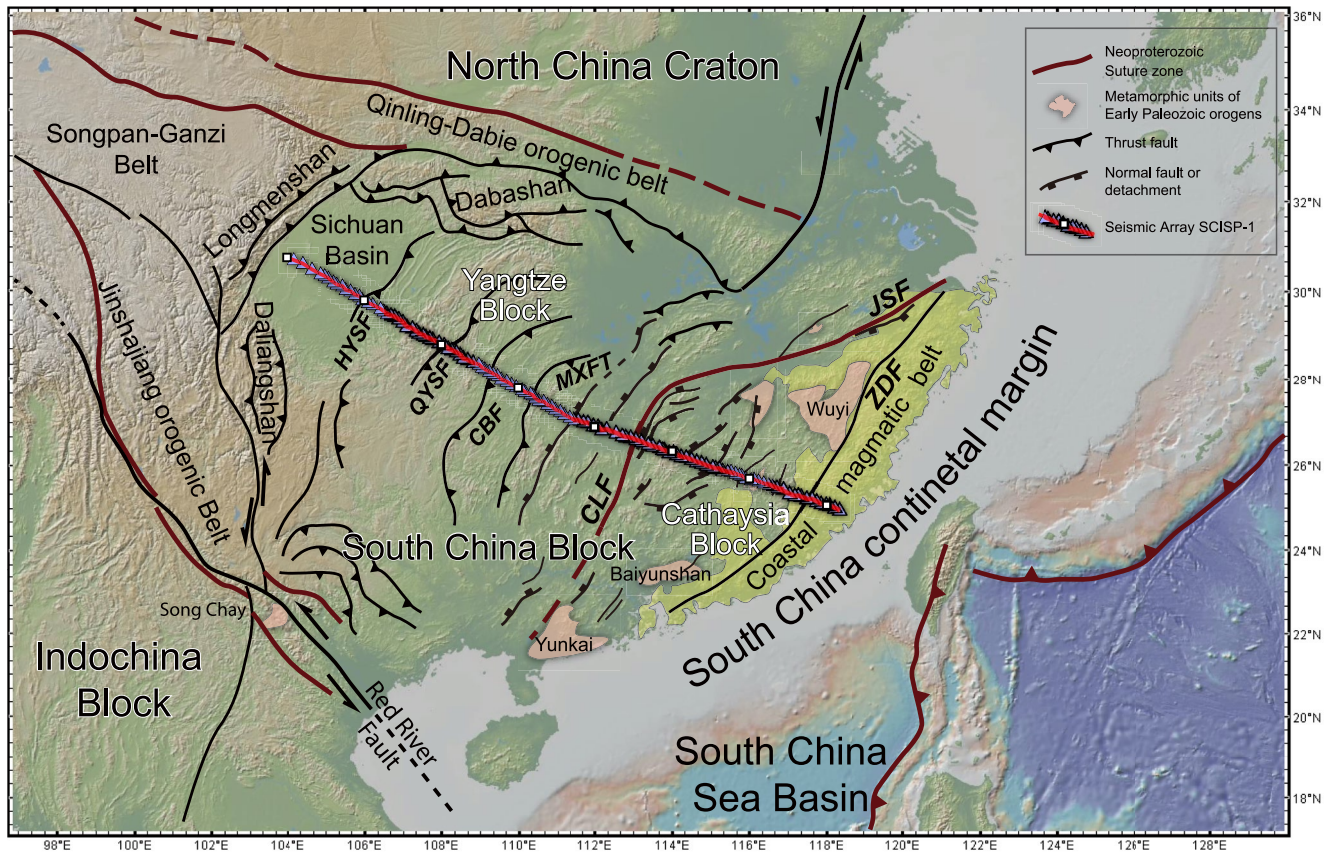
Figure 1. Tectonic map of South China (modified from Chu et al., 2019) and the locations of the array SCISP-1. The blue triangles represent the seismic stations. The white solid squares mark the longitude intervals along the profile. The abbreviations are: HYSF-Huayingshan Fault; QYSF-Qiyueshan Fault; CBF-Cili-Baojing Fault; MXFT-Main Xuefengshan Thrust; CLF-Chenzhou-Linwu Fault; JSF- Jiangshan-Shaoxing Fault; ZDF-Zhenghe-Dapu Fault.

(Li et al., 2010; Yao et al., 2012); widespread intracontinental orogenesis and the Basin-and-Range style tectonics and associated magmatism (Chu et al., 2012; Feng et al., 2022; Li & Li, 2007; Wang & Shu, 2012); and intensive extension and magmatism in the late Mesozoic and Cenozoic (Chu et al., 2019; Zhou et al., 2012).

A comprehensive understanding of the SCB's tectonic evolution requires deep and direct constraints from its lithosphere, as highlighted in the synthesis paper by Zhang et al. (2013). This necessitates obtaining better images of the deep lithospheric architecture, which has been made possible through the use of advanced deep geophysical models and new high-density data. In fact, recent models have provided highly detailed information on the crustal structures within the interior of the SCB. For example, Deng et al. (2011) collected wide-angle reflection/refraction seismic data and constructed a three-dimensional crustal velocity model of the SCB, which revealed laterally varying structural domains across the SCB. Deep reflection profiles across the SCB found significant dipping structures that may be associated with episodes of amalgamations in its tectonic history: the Panxi-Hannan subduction of along the NW and west margins of the Yangtze Block (Gao et al., 2016); the collision of the Yangtze and Cathaysia blocks beneath the Jiangnan Orogen (Dong et al., 2015); the assembly of the Wuyi and Coastal terranes in East Cathaysia (Dong et al., 2020). In a joint integration approach that combined recent available geophysical models, Li et al. (2022) presented the Rayleigh wave dispersion inversion and receiver function stacking results from the SCISP-1 line (see below), and found several wedge-like structures in the crust and shallow lithospheric upper mantle in the central SCB. These structures were interpreted to mark relict collision zones in the assembly of the Proterozoic SCB (Li et al., 2022).

3. Love Wave Data and Transdimensional Inversions

The three-component waveforms we used are from SCISP-1 (Figure 1), one of the South China Interior Structure Projects. The array was deployed from December 2009 to November 2013. With an average station spacing
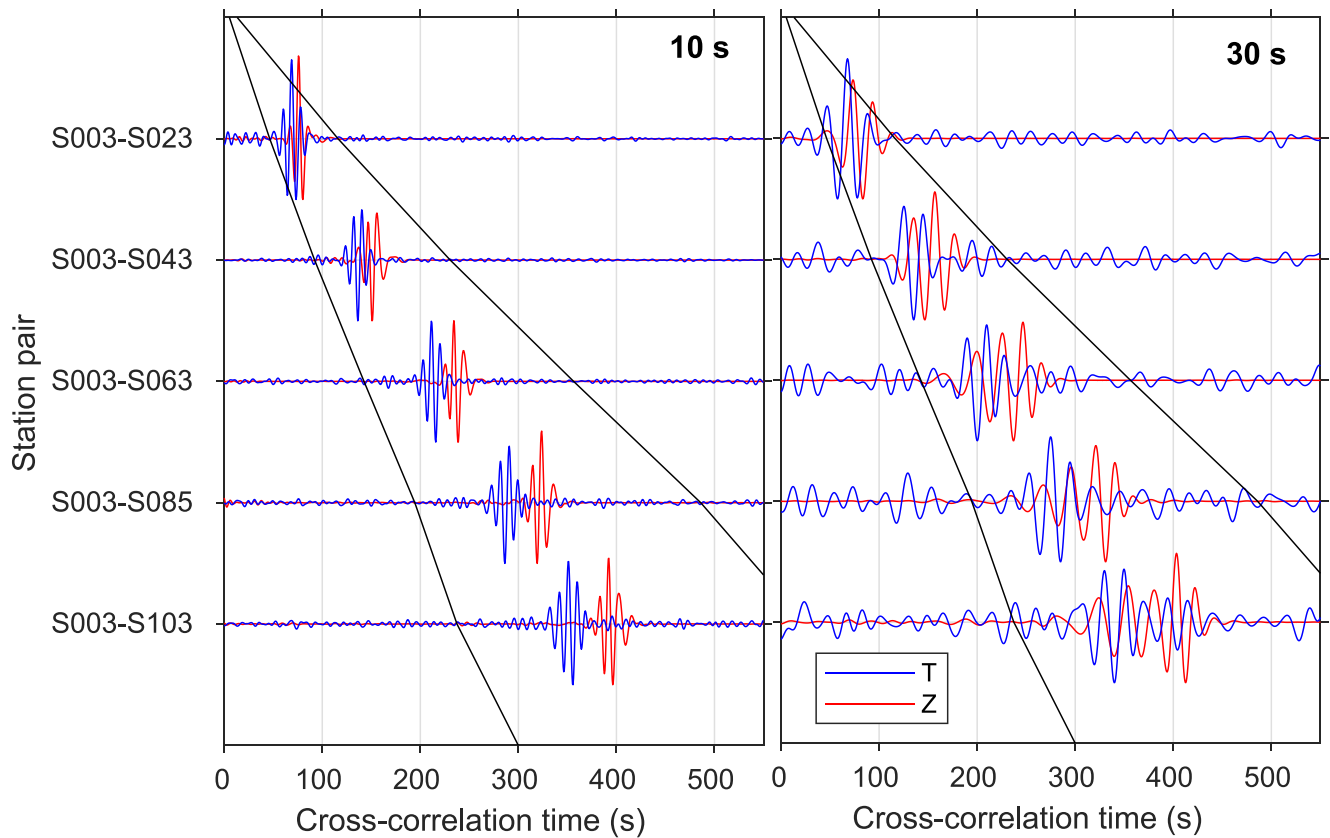
Figure 2. Examples for folded Rayleigh (Z) and Love (T) wave CCFs between southeastern-most station S003 and selected stations. Left panel: filtered with a 10 s central period Gaussian filter; right panel: with a 30 s central period Gaussian filter. Black lines show the empirical Love data window defined by moveout times determined by 2.0- and 5.0 km/s velocities.

of 15 km, this 1,500 km-long array started in the western Sichuan Basin and extended southeast in the Coastal magmatic belt (Figure 1). Broadband (up to 120 s) CMG-3ESP and 3T sensors and RefTEK-72A and 130 dataloggers were used to record continuous 3-component waveforms at a 40 Hz sample rate (see details in Li et al., 2022). In preparing the Love wave data, we followed the approach described in Li et al. (2022) where Rayleigh wave dispersion analysis was conducted. First, one-day-long horizontal waveforms were down-sampled to 5 Hz and cut into half-day long windows. For each window the mean, trend and instrument response were removed, and a band-pass Butterworth filter of 1–100 s applied. In addition, normalization with the running-absolute-mean method in both time and frequency domains was applied to suppress the earthquake signals. Then T-T cross-correlation functions (CCFs) were obtained using a phase weighted stacking method (Schimmel et al., 2011). The stacked CCFs were generally asymmetric (e.g., Fig. S2 in Li et al., 2022), which indicates dominant noise energy is from the southwest (the South China Sea). The CCFs were subsequently folded between the positive and negative components to obtain the symmetric CCFs. Figure 2 shows examples of such CCFs between station S003 and selected stations across the profile.

In Li et al. (2022) and this study, both Rayleigh and Love phase velocity dispersion curves were obtained through the Automatic Frequency-Time Analysis method (AFTAN; Bensen et al., 2007; Levshin et al., 1972). The AFTAN code uses a reference phase velocity model (here based on predictions from the 1D PREM model) to determine the correct phase velocity branch. Some constraints were defined to pick reliable phase velocity dispersion measurements. First in Li et al. (2022) we set the distance between station pairs to be greater than twice the wavelength for the Rayleigh waves. Given that horizontal data is usually poorer in quality than vertical data, resulting in fewer useable Love wave measurements, the minimum inter-station distance was set at 1.5-times wavelength. Secondly, the signal-to-noise ratio (SNR; defined in AFTAN) must be greater than 20. Finally, the phase velocity was set to be picked between 2 km/s and 5 km/s empirically along the line (Figure 2). We picked 2–36 s Love wave dispersion curves due to smaller SNRs, in contrast with the 5–60s range of the Rayleigh wave dispersion in Li et al. (2022). Figure 3 summarizes the Rayleigh and Love wave datasets.
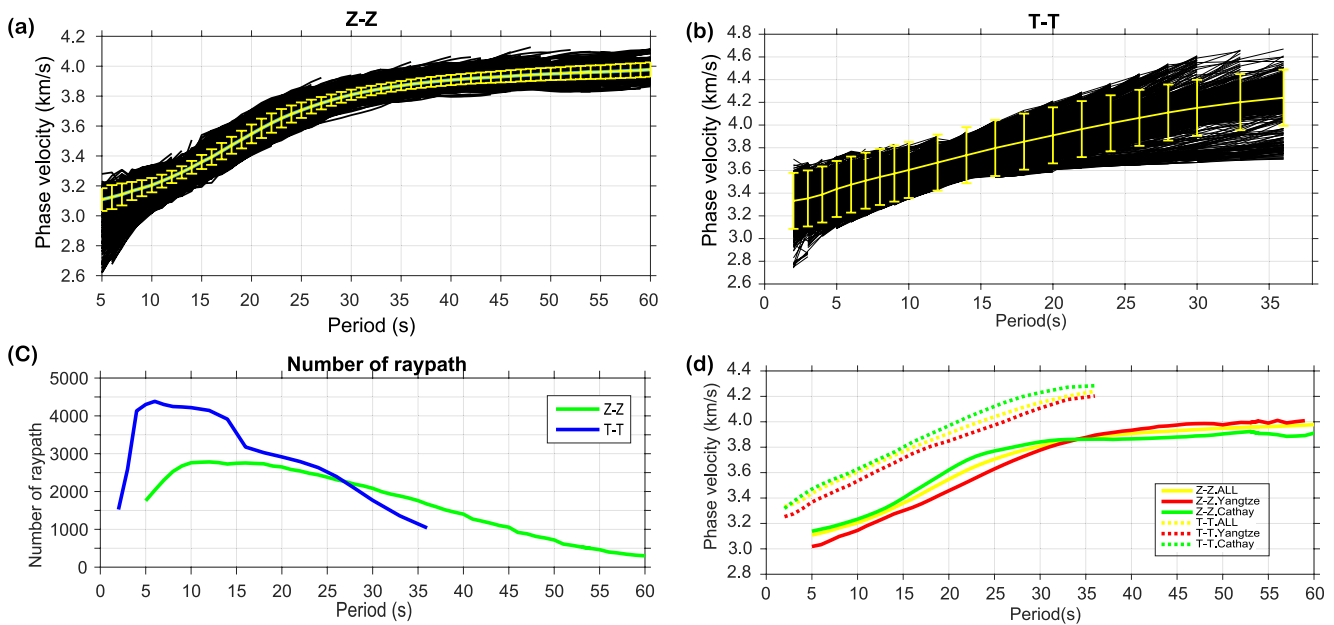
Figure 3. (a) Phase velocity dispersion curves of vertical (Z–Z) component; (b) Same as (a) but for horizontal (T–T) component; (c) Number of raypaths for Z-Z (green) and T-T (blue) component, separately; (d) Mean phase velocity along the Yangtze Block (red), Cathaysia block (Cathay, green) and the whole array (yellow). Solid line: Z-Z component; dashed line: T-T component. Error bars in (a) and (b) show the one-standard deviation of the measurements for corresponding periods.

We applied a two-step Bayesian transdimensional tomographic approach to invert the dispersion data for the final crustal models. In the first step the Love wave dispersion data among all available station pairs was inverted using a two-dimensional transdimensional tomography (Bodin & Sambridge, 2009) to obtain two-dimensional Love wave phase velocity models. In the second step, we conducted a joint inversion that combined the 2D Rayleigh wave maps obtained in Li et al. (2022) and the Love wave dispersion models to obtain simultaneously the isotropic velocity and radial anisotropy models with respect to depth. The two-step inversion procedures are consistent with those described in Li et al. (2022; also see Text S1 in Supporting Information S1), with two major differences that the Love wave data was inverted in this study; and both Rayleigh and Love wave dispersion maps were jointly inverted for isotropic velocity and radial anisotropy. Below we briefly discuss these major processing differences.

In the first step, a two-dimensional reversible jump tomographic method (Bodin & Sambridge, 2009) was applied, wherein the parameters of the model are defined by the nuclei of Voronoi cells. For each period, ray paths were calculated using the fast-marching method (FMM, Rawlinson & Sambridge, 2005). The prior model was set as a laterally homogeneous model based on the mean value of dispersion measurements for each period. Following the ray paths, synthetic travel times were calculated based on the randomly perturbed velocity model. The misfit between the data and synthetics decides whether the perturbed model was accepted or rejected. The posteriori models were produced using Bayes' theorem, and were stochastically generated via Markov chain Monte Carlo method. After the first iteration in which a new phase velocity model was obtained, we updated the ray paths with the FMM to consider ray bending due to large 2D velocity variations in the inverted crustal model. We iterated this inversion procedure two more times to obtain the final phase velocity model. For each period, the Love wave data set was inverted to reconstruct a 2D continuous phase velocity map in a rectangular model region, with the lower right corner at 25°N and 119°E and the upper left corner at 31°N and 104°E, using a grid size of 0.5°. For each period, 288 chains (or CPUs) were used to search for the velocity model. Initially, 10,000 initial search (burn-in) steps were conducted so that the search could start to converge. After that an additional 20,000 samples were searched for each chain (or CPU). A total of 5,760,000 (20,000 × 288) models form the resulting ensemble of searched models, from which the mean and standard deviation were derived for the Love wave phase velocity maps in the 2–36 s period range. Considering the linear nature of the station locations and raypath distribution, we transected the Love wave phase velocity model and model error along the SCISP-1 array (Figure 4). Figure 4b shows the corresponding model error determined by the inversion: smaller model uncertainties are presented between 2 and 25 s, while in the longer periods, the model errors become larger, especially over 30s due to limited ray coverage.
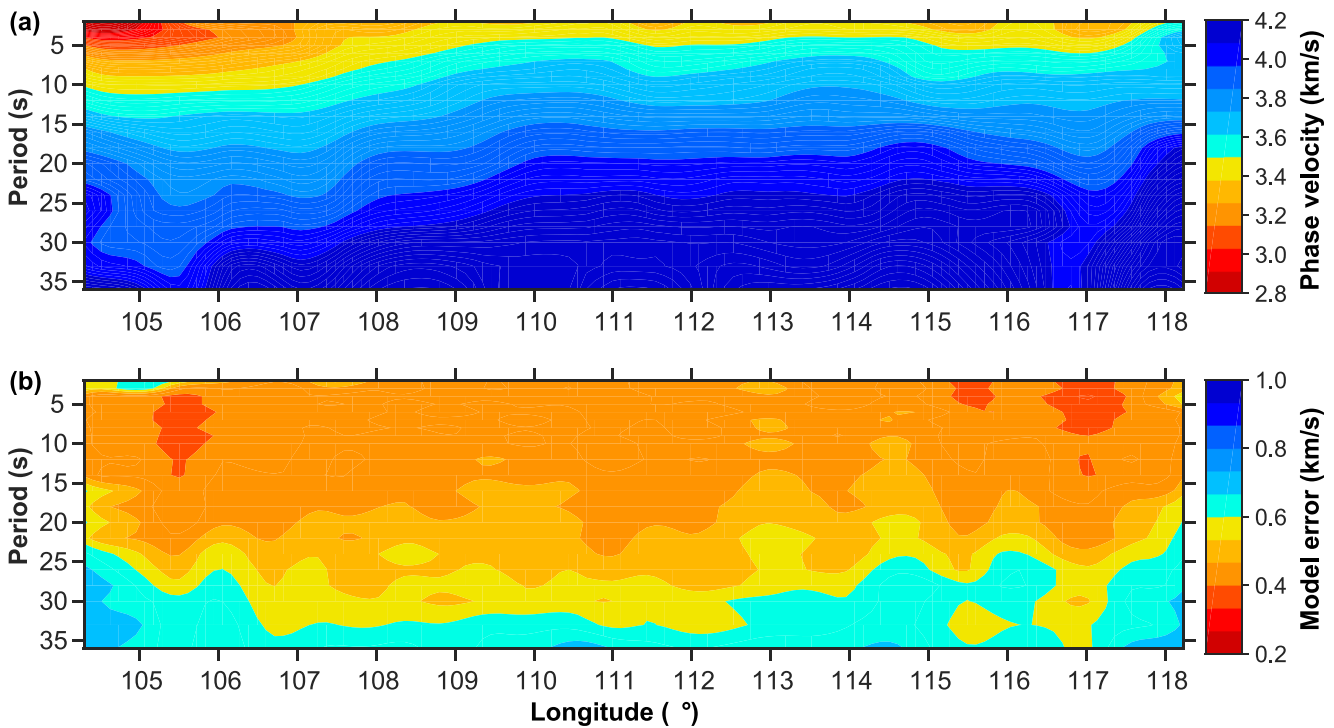
Figure 4. The 2–36 s Love phase velocity results along the profile. (a) Love phase velocity model; (b) model error along the SCISP-1. Note that the model errors are determined by the standard deviation of the ensemble of searched models.

In step two of the inversion, the dispersion model extracted at each location along the SCISP-1 line was inverted to depth, and all inverted 1-D profiles were combined together to form the final model. Here both Rayleigh phase velocity of 5–50s (Li et al., 2022) and Love phase velocity of 2–36 s were jointly inverted for isotropic shear wave velocity (V_s) and radial anisotropy (ξ) at each model grid. The tomographic method is based on the 1D trans-dimensional Bayesian algorithm used in our previous work (Li et al., 2022; Yuan & Bodin, 2018). Similarly, the inversion is based on a Bayesian formulation, and the model solutions are defined by a large number of Voronoi cells for velocity variation, layer thickness and the number of layers. The reference crustal V_s model was constructed using a smooth regional velocity model. This is in contrast to a wide distribution of background velocity models (usually from 2.0 to 5.0 km/s for crustal studies; Bodin et al., 2012), and can be achieved by adapting smooth continental velocity models or available local active-source models which are usually independent of the dispersion datasets used in our approach. Yuan and Bodin (2018) demonstrated that this approach guides the inversion to quickly converge. One advantage of the algorithm is that the approach avoids a subjective choice of damping and regularization, which would otherwise lead to biases when estimating the radial anisotropy ξ (Equation 2 below). Additionally, the number of model layers is a free parameter which is determined by the data and inversion (Bodin et al., 2012; Yuan & Bodin, 2018). We modified the inversion code to perform a joint inversion of both Rayleigh and Love wave dispersion data, which are sensitive to vertically polarized shear wave velocity (V_{sv}) and horizontally polarized shear wave velocity (V_{sh}), respectively. In the algorithm, the isotropic V_s and radial anisotropy ξ are given by V_{sh} and V_{sv} below (e.g., Panning & Romanowicz, 2006):

$$V_s^2 = \frac{2V_{sv}^2 + V_{sh}^2}{3} \tag{1}$$

$$\xi = \frac{V_{sh}^2}{V_{sv}^2} \tag{2}$$

4. New Radially Anisotropic Model Across the SCB

Figure 5 presents the new isotropic V_s and radial anisotropy ξ models and their associated errors. The starting V_s model that was constrained by the Rayleigh wave phase wave velocities in Li et al. (2022) is also presented in Fig.
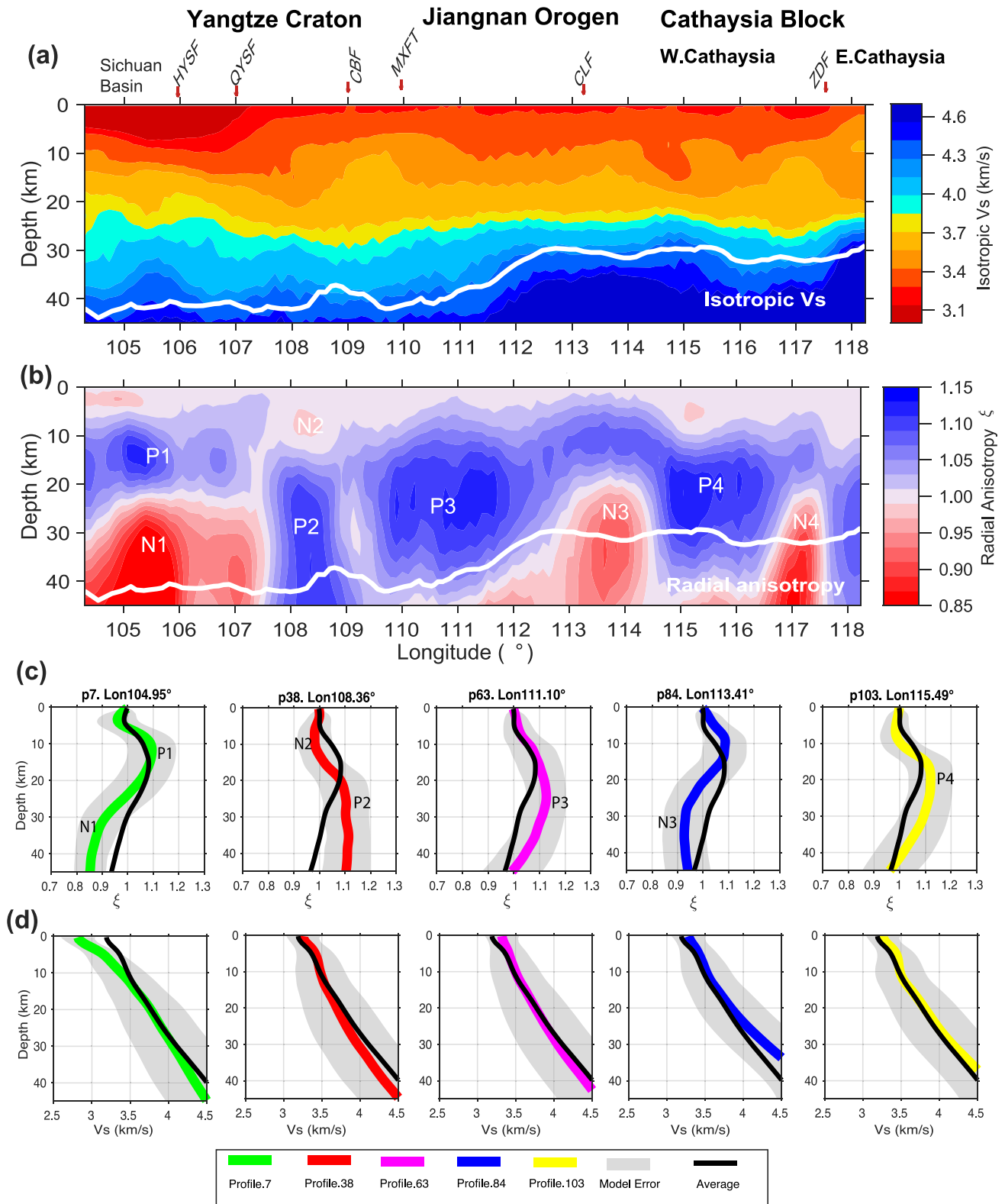
Figure 5. Seismic models along the SCISP-1 line. (a) Isotropic velocity V_s model; (b) Radial anisotropy model. The thick white line indicates the Moho estimated from receiver functions (Li et al., 2022). (c) Selected 1D radial anisotropy profiles and model errors (gray-shaded) which correspond to negative (N1–N3) and positive radial anisotropy (P1–P4) features which are discussed in the next section. For comparison, the average radial anisotropy along the whole profile is plotted. (d) same as (c) but for 1D isotropic Vs profile.

S4c,d in Supporting Information S1. It is worth noting that the dispersion dataset used in Li et al. (2022) model is more sensitive to the vertically polarized shear wave velocity (V_{sv}) structure, and here by combining the Love wave dataset which is sensitive to horizontally polarized shear wave velocity (V_{sh}) structure, the final velocity model depicts both isotropic and radial anisotropy models. This may result in slight differences between the two velocity models (Figure 5a, Figures S4 and S5 in Supporting Information S1), such as in the shallow crust of the northwest Sichuan Basin and mid-crust in the Cathaysia Block.

Overall, the new isotropic V_s model shows features that may spatially correlate with the surface geology: for example, the Sichuan Basin has very low velocities in the upper crust (<10 km depth) but high velocities in the mid-to lower crust (>25 km depth; Figures 5a and 5d); this high-velocity mid-to lower crust extends to nearly 112° longitude where the Moho as constrained by receiver functions (Li et al., 2022) shows a rapid transition from over 40 km depth in the Yangtze Block to ∼30 km depth in the Cathaysia Block. The mid-crust (∼10–25 km depth) of the eastern Yangtze Block has relatively high velocity, which extends toward south into the Cathaysia Block.

The new radial anisotropy model ξ clearly shows a strong spatial segmentation across the SCB. The Yangtze Block can be split into two blocks, one beneath the Sichuan Basin with positive ξ in the mid-crust (feature P1) and negative ξ in the lower crust (feature N1), and the other in east Yangtze and the Jiangnan Orogen which has a relatively weak ξ (close to 1) in the upper to mid-crust (0–10 km depth from 107° to 112.5° longitude) but a positive ξ in the mid-to lower crust (features P2 and P3). Note that we have used the Chenzhou-Linwu fault (Figure 1, CLF) as the terrane boundary between the Jiangnan Orogen and the Cathaysia Block, which was constrained by multiple datasets in Li et al. (2022). The Cathaysia Block has a strong positive ξ in the mid-to lower crust (Feature P4), which is truncated by two large negative ξ anomalies beneath the CLF and Zhenghe-Dapu fault (ZDF). The anisotropy features discussed have characteristic spatial sizes that are well above the resolving limit ∼0.4–0.6° shown in the resolution tests (Figs. S2–S3 in Supporting Information S1), suggesting that they are robust features.

5. New Crustal Constraints and Tectonic Interpretations

The interior of the SCB is currently characterized by nearly uniform GPS speed, coherent internal strain rate, and weak seismicity (Wang & Shen, 2020; Xu, 2001). These observations suggest a lack of internal deformation, implying that the lithosphere of the SCB is stable and its physical conditions are uniform. However, recent geophysical studies show a fundamental difference in both the crustal structure and lithospheric thickness across the SCB (e.g., Figure 5 in Li et al., 2022); in addition, since the amalgamation of the SCB, its interior has experienced drastically different tectonic processes that resulted in the cratonization and subsequent sedimentation in the Yangtze Block, and intracontinental orogeneses which were largely in the Cathaysia Block (Zhang et al., 2013). These observations suggest that a fundamental difference exists in the internal lithospheric architecture across the SCB, which may well be reflected in the new crustal model. Here we combine the isotropic V_s, radial anisotropy ξ, and the receiver function Common Conversion Point (CCP) model in Li et al. (2022) to jointly interpret the crustal seismic features in the framework of lithospheric deformation processes through the SCB tectonic history.

Given the large crustal thickness variations from the Sichuan Basin (∼40 km depth) to the Cathaysia Block (∼30 km depth), we construct a composite reference isotropic Vs model (Fig. S6 and Text S3 in Supporting Information S1) and compute V_s perturbations based on it (Figures 6–8). The ξ variations are with respect to isotropy (e.g., ξ = 1.0 or $V_{sh} = V_{sv}$), such that positive and negative variations may be simply linked to deformations in the horizontal and vertical sense, respectively. We then compare lateral structures in both Vs and ξ at the whole crustal levels across the SCB.

5.1. Strong Stratification and Fossil Subduction Beneath the Sichuan Basin

Evidenced by the surrounding thrust faults, for example, the Longmenshan Fault to the northwest, the Dabashan to the northeast, the Daliangshan to the south, and the Qiyueshan Fault (QYSF) to the east (Figure 1), the lithosphere underlying the Sichuan Basin may have undergone sustained deformation associated with the prolonged collisional processes along its margins, but internally a thick root has remained (Zhang et al., 2018). As a part of the Yangtze Block, the Sichuan Basin is covered by over 10 km thickness of Late Proterozoic to Quaternary sedimentary deposits (Wang et al., 2016). This is consistent with the strong velocity perturbation found (feature L1) in the new isotropic V_s model in the upper crust (Figure 6b).
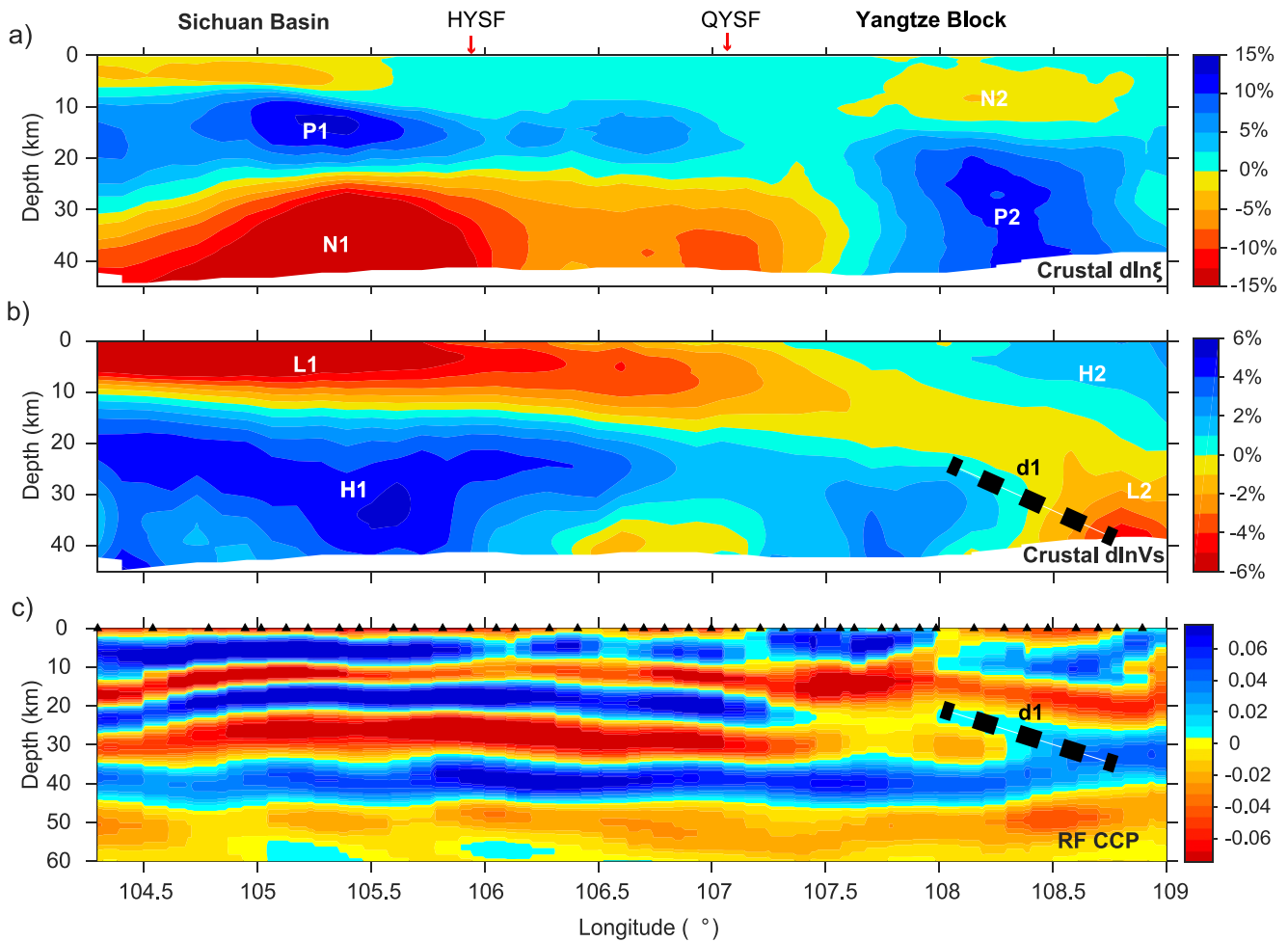
Figure 6. Model perturbations for the Yangtze Block. (a) radial anisotropy variation with respect to isotropy. (b) isotropic V_s perturbation with respect to the composite reference model (Fig. S6 in Supporting Information S1). (c) Receiver function CCP stacking model (Li et al., 2022) showing the vertical velocity gradient. Dashed black line shows the dipping interface inferred from receiver function CCP model.

The radially anisotropic model of the Sichuan Basin exhibits a distinct pattern of vertical stratification, which corresponds well with the two positive velocity gradients around ~5 and 15–20 km depth found in the receiver function CCP model (see Figure 6c). The negative radial anisotropy in the upper crust is strongly correlated with the deepening of the Quaternary and Mesozoic basins to the west (Wang et al., 2016). This contrasts with the normal positive anisotropy signal that typically results from flat-lying basin stratifications. The middle crust (10–25 km depth) is characterized by a large positive anisotropy feature (P1), which may spatially extend eastward into the QYSF. We attribute this positive anisotropy signal to the Sichuan Basin basement. The positive signal is typical of continental mid-crust, where the signal is attributed to the CPO- and/or SPO-induced anisotropy of mica-bearing rocks (Almqvist & Mainprice, 2017; Lloyd et al., 2009). According to Xie et al. (2013), the occurrence of planar mica sheets is a plausible explanation for the presence of positive mid-crustal radial anisotropy beneath eastern Tibet and the Sichuan Basin. West of the HYSF, the positive anisotropy signal may be reinforced by sedimentation of the Sichuan Basin.

Beneath the Sichuan Basin, a large negative radial anisotropy ($V_{sv} > V_{sh}$) domain is dominant in the lower crust (feature N1), which broadly correlates with the high velocity feature (H1) which may extend southeast of the QYSF. Negative anisotropy in the lithosphere can be attributed to active upwelling melts (plumes), ongoing subduction slab, vertically (or sub-vertically) aligned fossil structures (large scale faults). These structures can form the effective CPO or SPO that would lead to greater V_{sv} than V_{sh} and therefore negative ξ. We may rule out present-day active upwelling because the lithospheric thickness of the Sichuan basin reaches over 200 km, suggesting that this is a stable continent that may have protected the crust from deeper modification. We note that west of the HYSF, Gao et al. (2016) shows that south-east dipping reflectors cross the Moho and extend into the sub-crustal lithosphere,

which they interpreted as the relics of the Neoproterozoic Panxi-Hannan subduction along the NW margin of the Yangtze Block (Zhou et al., 2002). The reflection model also shows that these dipping reflectors extend into the lower crust (Figure 2b in Gao et al., 2016). The SCISP1 receiver function Common-Conversion-Point (CCP) image (Li et al., 2022) shows two dipping interfaces (at depths below 50 km around 105–105.5° and 105.9–106.3°), which spatially coincide with a upper mantle dipping reflector found in Gao et al. (2016). Gao et al. (2016) proposed that the western Yangtze margin experienced a series of fossil subductions and the marginal lithosphere expanded through outward accretions of the subducted lithosphere. Strong CPO usually exists within a subducting lithosphere (Park & Levin, 2002), with the anisotropy fast-axis direction parallel to the subduction direction. When accreted to the western Yangtze margin, a plunging fast axis direction would develop, leading to faster V_{sv} than V_{sh}, and therefore causing an negative radial anisotropy signal. A similar proposal for fossil subduction with plunging fast axis is found in shear-wave splitting and body-wave tomographic studies along the southern margin of the Wyoming Craton in North America (Fox & Sheehan, 2005; Yuan & Dueker, 2005). In addition, dipping subduction interfaces would also lead to dipping structural anisotropy (SPO), which would reinforce the signal from the "frozen-in" CPO anisotropy in accreted lithosphere. We therefore suggest that the strong negative anisotropy (N1) beneath the western Sichuan Basin is likely of a fossil subduction/accretion origin. Gao et al. (2016) further showed that the dipping interface extended into the mid- and lower crust. We suggest that both CPO- and SPO-induced anisotropy due to sub-vertical alignment of fossil fabrics may cause negative radial anisotropy N1 in the Sichuan Basin.

In the western Yangtze Block, a surface wave tomography study by Liu et al. (2021) revealed a northeast-trending negative radial anisotropy pattern between the mid-crust and ~80 km depth in the topmost sub-crustal lithospheric mantle. Liu et al. (2021) attributed the negative anisotropy, embedded in high shear-wave velocities, to a hidden fossil hotspot track that may potentially be responsible for the Late Permian Emeishan Large Igneous Province (ELIP) centered at the southwest corner of the Yangtze Block. Through the proposed plume passage, consolidated mafic-ultramafic dike-forming magma systems were expected to form high seismic velocity and negative radial anisotropy. It is noteworthy that the proposed hotspot track, if true, is spatially coincident with the feature N1, therefore consolidated vertical dikes could also be a viable candidate to form the negative radial anisotropy N1. A recent shear-wave splitting study, however, suggested that the plume impinging may be confined to the center of the ELIP (Li, Chen, et al., 2021). Tracing such hidden hotspot tracks thus may require finding more evidence of seismic signatures associated with plume-related modification of continental lithosphere (Sleep, 1990), for example, reduced velocities (e.g., Stachnik et al., 2008), high attenuation (Chu et al., 2013), and thinning of the lithosphere (Heyn & Conrad, 2022) reported in similar studies worldwide.

5.2. Rapid Lateral Change in Anisotropy in Eastern Yangtze

In the eastern Yangtze Block, the radial anisotropy domain quickly switches signs across the QYSF. Feature P2 denotes a prevailing pattern of positive radial anisotropy in the mid-to lower crust, which is overlain by a small negative ξ (feature N2) in the upper crust. The V_s model changes the pattern as well following the radial anisotropy, from the high velocity Sichuan Basin lower crust (H1) to a relatively low-velocity zone (L1). A broad NW up-dipping mid-to lower crustal interface (positive velocity gradient d1, Figure 6c) was previously imaged in the receiver function CCP model (Li et al., 2022). This feature spatially coincides with a highly conductive zone of crust and shallow sub-crustal lithospheric mantle, which is imaged in a magnetotelluric study (Zhang et al., 2015). Considering the thick lithosphere in the region, Li et al. (2022) suggested that d1 marks a relict suture zone which may have resulted from a Paleoproterozoic orogenic event predating the Jiangnan Orogeny (Cawood et al., 2020; Dong et al., 2015).

In the eastern Yangtze Block, a Mesozoic thin-skinned fold-and-thrust system (Yan et al., 2003) was developed in the upper crust east of the Huayingshan Fault (HYSF). Across the Qiyueshan Fault (QYSF), the system evolves into a thick-skinned pattern with V-shape syncline zones with more steeply dipping mid-to lower crustal faults (Yan et al., 2003). These thin-skinned and thick-skinned structural patterns are well reflected in reflection profiles of the eastern Yangtze Block (Dong et al., 2015; Li et al., 2018), and may cause SPO-induced radial anisotropy accordingly: for example, positive anisotropy due to flat-lying faults in the thin-skinned deformation zone in the upper crust between the HYSF and QYSF, and negative anisotropy (N2 in Figure 6a) due to steeply dipping faults in the upper and mid-crust of the eastern Yangtze. We attribute the transition in the upper to mid-crust radial anisotropy from positive to negative east of the QYSF (feature N2) to the change in orientation of foliation planes from horizontal (thin-skinned) to sub-vertical (thick-skinned), correspondingly.

In the mid-to lower crust, the large positive radial anisotropy feature (P2) lies above the dipping interface d1 (Figure 6b). Li et al. (2022) interpreted that this feature occurred before the Jiangnan Orogeny which assembled

the SCB, thus the crust east of d1 likely represents a proto-Yangtze block of at least late Paleoproterozoic age (Cawood et al., 2020). Positive radial anisotropy may be typical of cratonic mid-to lower crust (e.g., Dalton & Gaherty, 2013). Dalton and Gaherty (2013) attributed the strong radial anisotropy in the cratonic crust of western Canada to CPO of horizontally foliated and/or lineated mineral fabric, and/or strong isotropic velocity (or composition) layering in the mid-to lower crust.

5.3. Strong Anisotropy and Magmatic Intrusion in the Jiangnan Orogen

In the Jiangnan Orogen, strong positive anisotropy P3 at nearly the whole crust scale is most prominent, which is located mostly between the CBF and the CLF (Figure 1). Initially, the Jiangnan Orogen emerged as a result of the collision between the Yangtze and Cathaysia blocks. In the Early Paleozoic and Early Mesozoic, the suture belt was influenced by two intracontinental orogeny events (Faure et al., 2017; Yao et al., 2012). After orogenic collisions, the SCB experienced episodic extensions, due to the collapse post orogeny and the far-field effect of the (paleo-) Pacific subduction system (Chu et al., 2012, 2019; Li & Li, 2007). The extension and magmatism are clearly present in the coastal area, which further reached northwest into the MXFT (Chu et al., 2019).

The collisional zone between the Yangtze and Cathaysia blocks exhibits a rapid change in shear-wave velocity within the subcontinental lithosphere, which is attributed to a variety of factors that have led to significant variations in the lithospheric architecture. One possibility is the post-orogenic extension of the Jiangnan Orogeny, which could have resulted in lithospheric delamination and subsequent magmatic intrusion and mafic underplating in the Jiangnan orogenic crust. Another potential cause is the post-orogenic extension of two intracontinental orogenic events, which could have also contributed to lithospheric delamination and the formation of large-scale crustal faults. Additionally, extension due to roll-back of the Pacific plate may have played a role in the formation of large-scale faults and lithospheric delamination (e.g., Li & Li, 2007). These processes could have been enhanced by the presence of pre-existing large crustal-scale faults from earlier orogenies, as seen in the receiver functions (e.g., d2 and d3 in Figure 7c). The resulting changes in lithospheric architecture, including significant variations in the thickness of both the crust and lithosphere, may have contributed to the observed lateral variations in shear velocity within the subcontinental lithosphere.

Lower crustal magmatic underplating is frequently reported in Precambrian collision zones (Thybo & Artemieva, 2013). For our proposed fossil collision, after magma was injected into the lower crust, large positive ξ (P3, Figure 7a) may form in response to the magma fractionation and assimilation. After solidification, the injected magma may form horizontally aligned sill complexes or lenses (e.g., Yuan et al., 2010), which would manifest fast velocities (e.g., west of dipping structure d2 in Figure 7b) and a positive ξ signal in terms of SPO-induced anisotropy. It is also possible that CPO-induced anisotropy may occur in this case, due to the potential role of induced CPO of eclogites in lower crustal intrusions (Keppler, 2018). Induced CPO would further enhance the positive radial anisotropy. Unlike the feature P2 beneath the eastern Yangtze Block which is attributed to cratonic crustal basement, the large positive anisotropy (P3) here in the lower crust likely resulted from magmatic underplating, which may have been extensively developed after the Jiangnan Orogeny.

5.4. Positive Mid- and Lower Crustal Anisotropy and Crustal Extension in the CaB

The Cathaysia Block (CaB) is bounded to the west by the Chenzhou-Linwu fault (CLF) and extends southward to the Wuyi domain, crossing the ZDF to the coastal area. Its formation is the result of multiple stages of accretion since the Neoproterozoic period (Wang et al., 2014). The CaB has been heavily impacted by two intracontinental orogenies, the Indosinian and Yanshanian Orogenies, as evidenced by intense surface deformation, faulting, and magmatism (Li & Li, 2007; Wang & Shu, 2012; Zhou et al., 2012). This extensive surface deformation and granitic magmatism in the SCB have been referred to as the "Basin and Range Tectonics of South China" by Gilder et al. (1991). Recent deep imaging studies have shown that the CaB lithosphere has undergone significant thinning (Deng et al., 2019; Li et al., 2022; Wei et al., 2016; Zhang et al., 2018), and subsequent asthenospheric upwelling due to lithospheric extension has resulted in widely exposed Mesozoic granite and volcanic rocks in the eastern CaB (Deng et al., 2019; Li, 2000; Zhou et al., 2012). Additionally, the CaB developed widespread NE-SW trending faults (Cao et al., 2022; Wang et al., 2013), which could have provided potential channels for crustal melts.

The largest positive radial anisotropy of the entire SCISP-1 profile is observed in the mid-to-lower crust of the western Cathaysia Block (P4; Figure 8a). Similar to the widespread crustal positive radial anisotropy reported in the Basin and Range Province of the Western US (Moschetti et al., 2010), this strong anisotropy feature (P4) is readily
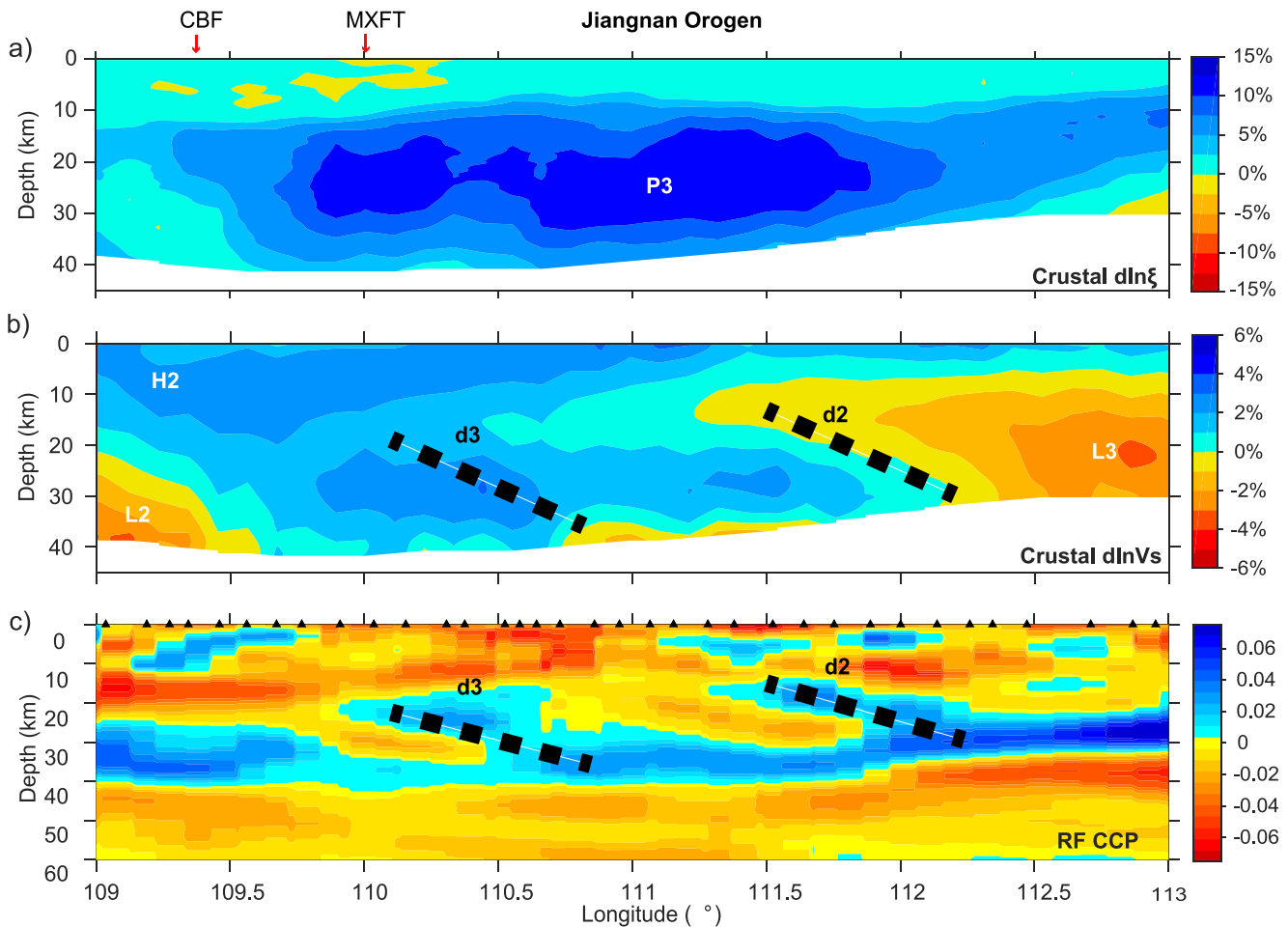
Figure 7. Model perturbations for the Jiangnan Orogen. (a) radial anisotropy variation. (b) isotropic V_s perturbation with respect to the composite reference model (Fig. S6 in Supporting Information S1). (c) Receiver function CCP stacking model (Li et al., 2022) showing the vertical velocity gradient. Dashed lines show the dipping interfaces (d2 and d3) inferred from receiver function CCP model.

attributed to the CPO-induced anisotropy of crustal anisotropic minerals in response to the regional extensional tectonics. In the western Cathaysia crust, the positive radial anisotropy is mostly concentrated in the mid-to-lower crust, where large velocity reductions are also observed in the velocity model (feature L4; Figure 8b). Based on previous H-k studies (e.g., Li et al., 2022; Wei et al., 2016), the average crustal composition of the Cathaysia Block is felsic. These seismic observations are consistent with a relatively weak, quartz-rich crust that facilitates ductile deformation in crustal extension, as proposed in the western US (Lowry and Perez-Gussinye, 2011). Li et al. (2022) further compared the low crustal V_s and transparent (lack of dipping interfaces) crustal receiver function signals here in the CaB with contrasting observations in the Yangtze crust, and attributed the differences to the long-term lithospheric responses of the two intracontinental orogenies. Due to the much thinner lithosphere of the CaB, the crust was more exposed to the diffuse deformation associated with Phanerozoic orogenesis, which may have eventually overwritten the original crustal deformation characteristics in the CaB.

5.5. Negative Anisotropy and Terrane Boundaries in the CaB

In the CaB, two intriguing negative radial anisotropy features (N3 and N4) are observed in the mid-to lower crust. N4 is located directly beneath the ZDF, while the northern edge of N3 is located under the CLF, which is conventionally considered as the boundary between the Yangtze and Cathaysia blocks (Wang et al., 2003). Negative radial anisotropy is typically attributed to near-vertical cracks or faults in the upper crust and steeply dipping or subvertical mica sheets in the mid-crust (Xie et al., 2013). In the CaB, an active-source imaging study (Dong et al., 2020) imaged the ZDF as a whole-crust fault system that divides West and East Cathaysia. The ZDF has a high angle fault plane in the lower crust, which could cause the negative radial anisotropy signal (N4). Infiltrating
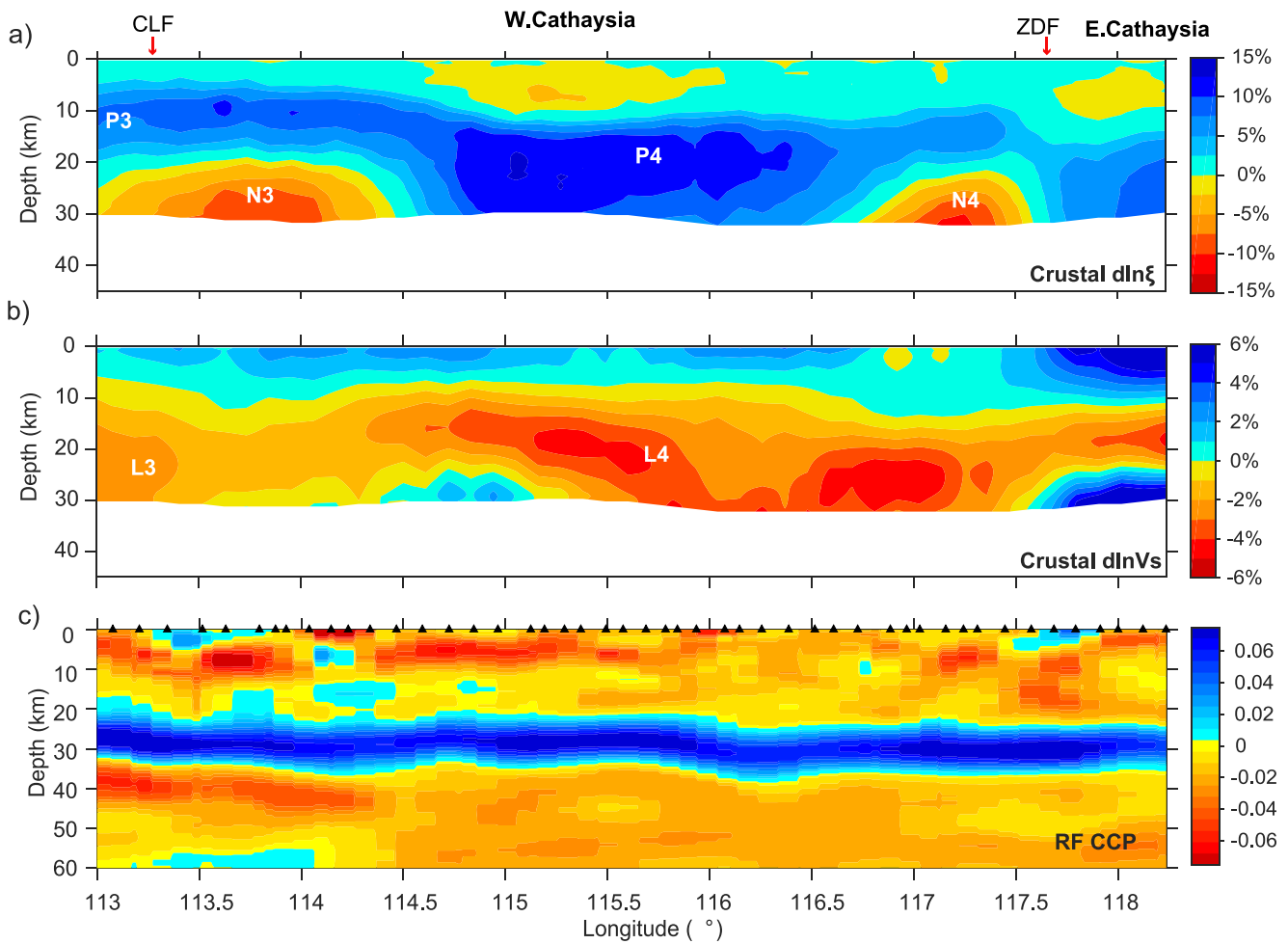
Figure 8. Model perturbations for the Cathaysia Block. (a) radial anisotropy variation. (b) isotropic V_s perturbation with respect to the composite reference model (Fig. S6 in Supporting Information S1). (c) Receiver function CCP stacking model (Li et al., 2022) showing the vertical velocity gradient.

melts may further strengthen the negative radial anisotropy signal by reinforcing the subvertical structure along the fault plane through melt transport or crystallization. Surface wave tomography shows that the thin lithosphere of the CaB may be perturbed by lower velocities, which may guide asthenospheric upwelling toward shallow fault systems (Fig. S7 in Supporting Information S1; Bao et al., 2015). We propose that the negative radial anisotropy observed beneath the ZDF might be attributed to the influence of ongoing upwelling processes.

The negative radial anisotropy structure N3 beneath the CLF in the CaB may be attributed to both a fossil collisional zone and present-day upwelling melts. Li et al. (2022) reported an over 200 km wide lithospheric suture zone immediately north of the CLF, which is characterized by rapid lateral change in both the Moho depth and lithosphere-asthenosphere boundary (LAB). This lithospheric suture zone may have resulted from the Jiangnan Orogeny, and edge-driven convection due to the large lateral difference in the LAB topography may create a large horizontal pressure gradient in the asthenosphere. This would promote repeated melt infiltration/upwelling into the weak lithospheric suture zone. The negative radial anisotropy anomaly observed in this area may therefore result from both the fossil collisional zone and the present-day upwelling melts.

5.6. Continental Fragments in the SCB

The new radial anisotropy model reveals significant lateral variations in seismic anisotropy across the SCB (Figure 5). Transitions from positive to negative crustal anisotropic domains are prominent and correlate well with large regional faults that are well-exposed at the surface. In contrast, the whole Yangtze Block shows a clear vertical stratification in the crustal radial anisotropy. Beneath the Sichuan Basin, the top crustal layer of positive
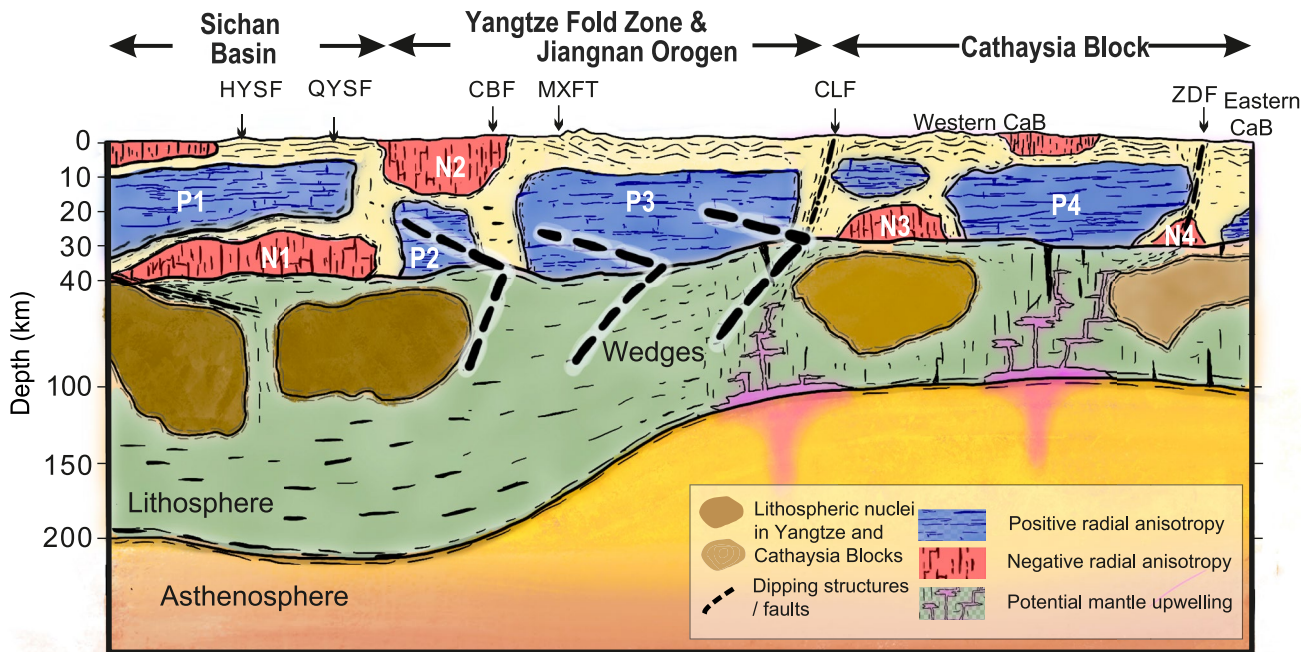
Figure 9. Fragmented continental blocks in the SCB resulted from its long tectonic evolution history, based on the conceptual lithospheric model of the SCB in Zhang et al. (2013) and further adapted by Li et al. (2022) which focused on the Proterozoic assembly of the SCB. Horizontal and vertical stripes with shading in the crust denote the radial anisotropy features: blue, positive anisotropy and red, negative anisotropy inferred from this study. Moho is from receiver function results in Li et al. (2022). Brown zones in the mantle lithosphere denote lithospheric nuclei inferred from a shear-wave tomographic model (Bao et al., 2015). Black dashed lines denote large crustal and sub-crustal faults inferred from previous studies (Dong et al., 2020; Gao et al., 2016; Wang et al., 2003) or the tectonic wedges (Li et al., 2022).

anisotropy is attributed to the thick sedimentary basin, while the negative anisotropy in the bottom layer results from the subduction that tilted the deformation fabrics preserved in the Panxi-Hannan arc lithosphere along the western and northern Yangtze margin. The radial anisotropy switches signs in the Yangtze fold zone, where the negative anisotropy in the upper layer is likely due to the thick-skinned fault systems, and the positive anisotropy in the bottom layer, located coinciding with the upper arm of a tectonic wedge, is interpreted to result from a Paleoproterozoic collision within the Yangtze Block (Cawood et al., 2020; Li et al., 2022). Clearly, the crust of the Yangtze Block is underlain by a thick cratonic lithosphere (Figure 9; Bao et al., 2015), which may have played a critical role in preserving these fossil deformation fabrics during the subsequent Jiangnan Orogeny and post-assembly intraplate orogenic processes of the SCB (e.g., Cawood et al., 2018).

Most of the CaB and Jiangnan Orogen, on the other hand, are dominated by a whole-crust positive radial anisotropy. In the CaB, this is attributed to the on-going Basin-and-Range style crustal stretching, characterized by the low crustal shear velocity, low Vp/Vs ratio (hence felsic crustal composition), thinned Cathaysia lithosphere and surface granitic magmatism, all of which collectively support this notion. In contrast, the whole-crust positive anisotropy in the Jiangnan Orogen (feature P3), which seems to be interconnected with that (P4) in the Cathaysia Block, is interpreted to be of a fossil collisional origin, which is supported by overall higher crustal velocity, dipping crustal interfaces and thicker lithosphere. The positive anomaly P4 is bounded by two lower crustal negative anisotropy features underneath the ZDF and CLF. These crustal faults may be further extended to the edges of two possible domains in the CaB lithosphere (shaded regions in Figure 9) in a regional surface wave tomography model (Bao et al., 2015). Magnetotelluric models of the CaB also display discrete domains with large resistivity in both crust and lithospheric mantle (Zhang et al., 2020). Taken together, the new geophysical observations suggest that the ZDF and CLF are deep-rooted lithospheric faults, which may further favor the model that the CaB has experienced accretion of multiple terranes, although the detailed evolutionary processes still remain debated (Lin et al., 2018; Wang et al., 2014).

The highly fragmented crustal domains revealed by the new SCB seismic model have important tectonic implications. Fragmented crustal domains with sub-parallel boundary faults are observed in various locations, including the western Superior Craton (Percival et al., 2006) and the Yilgarn Craton (Cassidy et al., 2006), both of which are part of stable Archean cratons, as well as in the eastern Tethys domain where the present-day

collision between the Indian plate and the Eurasian continent is taking place (Metcalfe, 2013; Wan et al., 2019). Clearly, such crustal fragments or terranes have played critical roles in assembling stable continental areas, but why they have survived various supercontinent cycles throughout the long span of Earth's tectonic evolution remains intriguing - geodynamic modeling shows that as inherited structures from previous tectonic activity, such crustal fragments likely control first-order deformation during initial continental rifting (Heron et al., 2016, 2023).

In the SCB, the deep lithospheric root beneath the Yangtze Block (Sichuan Basin) may have protected the crustal blocks from infiltration of asthenospheric melts, which can weaken the overlying lithosphere. Despite the presence of large-scale surface faults that clearly map the boundaries between crustal blocks, the lithosphere remains mechanically strong and does not break. However, petrological and geochemical observations of mantle xenoliths in the Early Mesozoic and Cenozoic alkaline rocks suggest that the lithosphere beneath the Cathaysia Block (about 80–90 km in thickness) is significantly thinner than in the Yangtze Block (more than 110 km; Liu, 2013), and the thermal-blanket effect does not apply. Variations in Sr-Nd isotopes of the late-Mesozoic mafic rocks in west Cathaysia and Jiangnan orogen show an age trend, from depleted mantle sources around 198–160 Ma to enriched lithospheric sources at 95–80 Ma (Yang et al., 2021; Zhang et al., 2023). Zhang et al. (2023) attributed this source transition to limited melting of the upwelling asthenosphere at 198-160 Ma and a progressive increase of partial melting of the lithospheric mantle from 160 to 140 Ma to 140–95 Ma, favoring lithospheric delamination and subsequent asthenospheric upwelling (Yang et al., 2021; Zhang et al., 2023). The fragmented continental pieces imaged in Figure 9 may have guided asthenospheric melts along internal boundaries toward the surface, leading to the Basin-and-Range style deformation and magmatism.

6. Concluding Remarks

The high-resolution seismic models of the SCB provide new insights into the lithospheric architecture and tectonic evolution of this region. Our analysis reveals the following key findings.

- The SCB displays strong lateral variations in seismic properties, indicating that it underwent assembly of multiple blocks or terranes, orogeny, and post-orogenic deformation.
- The Yangtze Block is characterized by ancient amalgamation features from the Paleoproterozoic to the Neoproterozoic, which have been preserved due to its thick lithospheric root. In contrast, the Jiangnan Orogen and Cathaysia Block have undergone significant deformations in the Phanerozoic, altering their anisotropy signature.
- The Jiangnan Orogen and Cathaysia Block show distinct positive anisotropy, indicating intense extensional deformation, but different origins. The Jiangnan Orogen experienced episodic post-orogenic extensions and magmatism, whereas the fabric of the Cathaysia Block can be attributed to ongoing Basin-and-Range style crustal extension.
- Whole-crust scale boundaries, such as the MXFT, CLF, and ZDF, are observed among the Yangtze, Jiangnan Orogen, and Cathaysia blocks. The interior of these blocks exhibits particular seismic characteristics of its own. We speculate that the boundary or suture zone plays an important role in controlling the later deformation tectonic activities.

Although the SCB currently appears to be characterized by uniform surface deformation and stress state, its tectonic evolution has been characterized by multi-block assembly, multi-orogenic events, and pervasive deformation. Based on our seismic models and other geophysical evidences, we propose that the anisotropic structures observed in the SCB may demarcate a set of continental fragments that were accreted through successive orogenic events. Such continental fragments exhibit different tectonic responses to long-term evolution (e.g., Heron et al., 2023; Gün et al., 2021), and our new multiscale seismic approach presented in this study illustrates its potential to provide deep constraints that can enhance comprehension of these processes.

Data Availability Statement

The raw cross-correlation function waveforms used to produce the new radial anisotropic model presented in this study for both Rayleigh waves (Z-Z component) and Love waves (T-T component) are available at Yuan et al. (2023) https://doi.org/10.6084/m9.figshare.22698181.v3.

References

Alder, C., Debayle, E., Bodin, T., Paul, A., Stehly, L., Pedersen, H., & Group, A. W. (2021). Evidence for radial anisotropy in the lower crust of the Apennines from Bayesian ambient noise tomography in Europe. *Geophysical Journal International*, *226*(2), 941–967. https://doi.org/10.1093/gji/ggab066

Almqvist, B. S., & Mainprice, D. (2017). Seismic properties and anisotropy of the continental crust: Predictions based on mineral texture and rock microstructure. *Reviews of Geophysics*, *55*(2), 367–433. https://doi.org/10.1002/2016rg000552

Anderson, D. L. (1961). Elastic wave propagation in layered anisotropic media. *Journal of Geophysical Research*, *66*(9), 2953–2963. https://doi.org/10.1029/jz066i009p02953

Bao, X., Song, X., & Li, J. (2015). High-resolution lithospheric structure beneath Mainland China from ambient noise and earthquake surface-wave tomography. *Earth and Planetary Science Letters*, *417*, 132–141. https://doi.org/10.1016/j.epsl.2015.02.024

Bensen, G. D., Ritzwoller, M. H., Barmin, M. P., Levshin, A. L., Lin, F., Moschetti, M. P., et al. (2007). Processing seismic ambient noise data to obtain reliable broad-band surface wave dispersion measurements. *Geophysical Journal International*, *169*(3), 1239–1260. https://doi.org/10.1111/j.1365-246X.2007.03374.x

Bodin, T., & Sambridge, M. (2009). Seismic tomography with the reversible jump algorithm. *Geophysical Journal International*, *178*(3), 1411–1436. https://doi.org/10.1111/j.1365-246X.2009.04226.x

Bodin, T., Sambridge, M., Tkal, H., Arroucau, P., Gallagher, K., & Rawlinson, N. (2012). Transdimensional inversion of receiver functions and surface wave dispersion. *Journal of Geophysical Research*, *117*, B02301. https://doi.org/10.1029/2011jb008560

Cao, L., Yuan, H., Zhao, L., Zhao, M., Huang, H., Hao, T., & Qiu, X. (2022). Fault-Controlled regional magmatism and mineral deposition in central Cathaysia—Evidence from ambient noise tomography. *Science China Earth Sciences*, *65*(9), 1715–1735. https://doi.org/10.1007/s11430-021-9941-2

Cassidy, K., Champion, D., Krapez, B., Barley, M., Brown, S., Blewett, R., et al. (2006). A revised geological framework for the Yilgarn Craton, Western Australia. *Geological Survey of Western Australia, Record*, *8*(8), 15.

Cawood, P. A., Wang, W., Zhao, T., Xu, Y., Mulder, J. A., Pisarevsky, S. A., et al. (2020). Deconstructing South China and consequences for reconstructing Nuna and Rodinia. *Earth-Science Reviews*, *204*, 103169. https://doi.org/10.1016/j.earscirev.2020.103169

Cawood, P. A., Zhao, G., Yao, J., Wang, W., Xu, Y., & Wang, Y. (2018). Reconstructing South China in Phanerozoic and Precambrian supercontinents. *Earth-Science Reviews*, *186*, 173–194. https://doi.org/10.1016/j.earscirev.2017.06.001

Cheng, C., Chen, L., Yao, H., Jiang, M., & Wang, B. (2013). Distinct variations of crustal shear wave velocity structure and radial anisotropy beneath the North China Craton and tectonic implications. *Gondwana Research*, *23*(1), 25–38. https://doi.org/10.1016/j.gr.2012.02.014

Chu, R., Leng, W., Helmberger, D. V., & Gurnis, M. (2013). Hidden hotspot track beneath the eastern United States. *Nature Geoscience*, *6*(11), 963–966. https://doi.org/10.1038/ngeo1949

Chu, Y., Faure, M., Lin, W., & Wang, Q. (2012). Early mesozoic tectonics of the South China block: Insights from the Xuefengshan intracontinental orogen. *Journal of Asian Earth Sciences*, *61*, 199–220. https://doi.org/10.1016/j.jseaes.2012.09.029

Chu, Y., Lin, W., Faure, M., Xue, Z., Ji, W., & Feng, Z. (2019). Cretaceous episodic extension in the south China block, east Asia: Evidence from the Yuechengling massif of central south China. *Tectonics*, *38*(10), 3675–3702. https://doi.org/10.1029/2019tc005516

Dalton, C. A., & Gaherty, J. B. (2013). Seismic anisotropy in the continental crust of northwestern Canada. *Geophysical Journal International*, *193*(1), 338–348. https://doi.org/10.1093/gji/ggs108

Deng, Y., Li, J., Peng, T., Ma, Q., Song, X., Sun, X., et al. (2019). Lithospheric structure in the Cathaysia block (south China) and its implication for the late Mesozoic magmatism. *Physics of the Earth and Planetary Interiors*, *291*, 24–34. https://doi.org/10.1016/j.pepi.2019.04.003

Deng, Y.-F., Li, S.-L., & Liu, J. (2011). Crustal structure beneath South China revealed by deep seismic soundings and its dynamics implications. *Chinese Journal of Geophysics*, *54*(10), 2560–2574.

Dong, S., Li, J., Cawood, P. A., Gao, R., Zhang, Y., & Xin, Y. (2020). Mantle influx compensates crustal thinning beneath the Cathaysia Block, South China: Evidence from SINOPROBE reflection profiling. *Earth and Planetary Science Letters*, *544*, 116360. https://doi.org/10.1016/j.epsl.2020.116360

Dong, S. W., Zhang, Y. Q., Gao, R., Su, J. B., Liu, M., & Li, J. H. (2015). A possible buried Paleoproterozoic collisional orogen beneath central South China: Evidence from seismic-reflection profiling. *Precambrian Research*, *264*, 1–10. https://doi.org/10.1016/j.precamres.2015.04.003

Faure, M., Chen, Y., Feng, Z., Shu, L., & Xu, Z. (2017). Tectonics and geodynamics of South China: An introductory note. *Journal of Asian Earth Sciences*, *141*, 1–6. https://doi.org/10.1016/j.jseaes.2016.11.031

Feng, Z., Chu, Y., Wei, W., Xue, Z., Xin, G., Meng, L., et al. (2022). Basal décollement splaying induces mid-crustal tectonic imbrication in an intracontinental orogen. *Tectonics*, *41*(12), e2022TC007583. https://doi.org/10.1029/2022tc007583

Fox, O., & Sheehan, A. F. (2005). Shear wave splitting beneath the CDROM transects. In G. Randy & K. E. Karlstrom (Eds.), *The rocky mountain region—An evolving lithosphere: Tectonics, geochemistry, and geophysics, geophysical monograph* (pp. 347–360). American Geophysical Union.

Fu, Y. V., Gao, Y., Li, A., Lu, L., Shi, Y., & Zhang, Y. (2016). The anisotropic structure in the crust in the northern part of North China from ambient seismic noise tomography. *Geophysical Journal International*, *204*(3), 1649–1661. https://doi.org/10.1093/gji/ggv549

Gao, R., Chen, C., Wang, H., Lu, Z., Brown, L., Dong, S., et al. (2016). SINOPROBE deep reflection profile reveals a Neo-Proterozoic subduction zone beneath Sichuan Basin. *Earth and Planetary Science Letters*, *454*, 86–91. https://doi.org/10.1016/j.epsl.2016.08.030

Gilder, S. A., Keller, G. R., Luo, M., & Goodell, P. (1991). Eastern Asia and the western Pacific timing and spatial distribution of rifting in China. *Tectonophysics*, *197*(2–4), 225–243. https://doi.org/10.1016/0040-1951(91)90043-r

Gün, E., Pysklywec, R. N., Göğüş, O. H., & Topuz, G. (2021). Pre-collisional extension of microcontinental terranes by a subduction pulley. *Nature Geoscience*, *14*(6), 443–450. https://doi.org/10.1038/s41561-021-00746-9

Heron, P. J., Peace, A. L., McCaffrey, K. J. W., Sharif, A., Yu, A. J., & Pysklywec, R. N. (2023). Stranding continental crustal fragments during continent breakup: Mantle suture reactivation in the Nain Province of Eastern Canada. *Geology*, *51*(4), 362–365. https://doi.org/10.1130/g50734.1

Heron, P. J., Pysklywec, R. N., & Stephenson, R. (2016). Lasting mantle scars lead to perennial plate tectonics. *Nature Communications*, *7*(1), 1–7. https://doi.org/10.1038/ncomms11834

Heyn, B. H., & Conrad, C. P. (2022). On the relation between basal erosion of the lithosphere and surface heat flux for continental plume tracks. *Geophysical Research Letters*, *49*(7), e2022GL098003. https://doi.org/10.1029/2022gl098003

Hu, S., Yao, H., & Huang, H. (2020). Direct surface wave radial anisotropy tomography in the crust of the eastern Himalayan syntaxis. *Journal of Geophysical Research: Solid Earth*, *125*(5), e2019JB018257. https://doi.org/10.1029/2019jb018257

Huang, H., Yao, H., & Van der Hilst, R. D. (2010). Radial anisotropy in the crust of SE Tibet and SW China from ambient noise interferometry. *Geophysical Research Letters*, *37*(21). https://doi.org/10.1029/2010gl044981

Keppler, R. (2018). Crystallographic preferred orientations in eclogites–A review. *Journal of Structural Geology*, *115*, 284–296. https://doi.org/10.1016/j.jsg.2018.04.003

Levshin, A. L., Pisarenko, V., & Pogrebinsky, G. (1972). *On a frequency-time analysis of oscillations*. Centre National de la Recherche Scientifique. paper presented at Annales de Geophysique.

Li, J., Dong, S., Cawood, P. A., Zhao, G., Johnston, S. T., Zhang, Y., & Xin, Y. (2018). An Andean-type retro-arc foreland system beneath northwest South China revealed by SINOPROBE profiling. *Earth and Planetary Science Letters*, *490*, 170–179. https://doi.org/10.1016/j.epsl.2018.03.008

Li, L., Zhang, X., Liao, J., Liang, Y., & Dong, S. (2021). Geophysical constraints on the nature of lithosphere in central and eastern Tibetan plateau. *Tectonophysics*, *804*, 228722. https://doi.org/10.1016/j.tecto.2021.228722

Li, T., Jiang, M., Zhao, L., Yao, W., Chen, L., Chu, Y., et al. (2022). Wedge tectonics in south China: Constraints from new seismic data. *Science Bulletin*, *67*(14), 1496–1507. https://doi.org/10.1016/j.scib.2022.05.007

Li, W., Chen, Y., Liang, X., & Xu, Y.-G. (2021). Lateral seismic anisotropy variations record Interaction between Tibetan mantle flow and plume-Strengthened Yangtze craton. *Journal of Geophysical Research: Solid Earth*, *126*(4), e2020JB020841. https://doi.org/10.1029/2020JB020841

Li, X.-h. (2000). Cretaceous magmatism and lithospheric extension in Southeast China. *Journal of Asian Earth Sciences*, *18*(3), 293–305. https://doi.org/10.1016/s1367-9120(99)00060-7

Li, Z.-X., & Li, X.-H. (2007). Formation of the 1300-km-wide intracontinental orogen and postorogenic magmatic province in Mesozoic south China: A flat-slab subduction model. *Geology*, *35*(2), 179. https://doi.org/10.1130/g23193a.1

Li, Z.-X., Li, X.-H., Wartho, J.-A., Clark, C., Li, W.-X., Zhang, C.-L., & Bao, C. (2010). Magmatic and metamorphic events during the early Paleozoic Wuyi-Yunkai orogeny, southeastern South China: New age constraints and pressure-temperature conditions. *Bulletin*, *122*(5–6), 772–793. https://doi.org/10.1130/b30021.1

Lin, S., Xing, G., Davis, D. W., Yin, C., Wu, M., Li, L., et al. (2018). Appalachian-style multi-terrane Wilson cycle model for the assembly of South China. *Geology*, *46*(4), 319–322. https://doi.org/10.1130/g39806.1

Liu, C. Z. (2013). Nature and formation age of the Phanerozoic sub-continental lithospheric mantle in South China. *Acta Petrologica et Mineralogica*, *32*(5), 637–651.

Liu, Y., Li, L., Van Wijk, J., Li, A., & Fu, Y. V. (2021). Surface-wave tomography of the Emeishan large igneous province (China): Magma storage system, hidden hotspot track, and its impact on the Capitanian mass extinction. *Geology*, *49*(9), 1032–1037. https://doi.org/10.1130/g49055.1

Lloyd, G. E., Butler, R. W., Casey, M., & Mainprice, D. (2009). Mica, deformation fabrics and the seismic properties of the continental crust. *Earth and Planetary Science Letters*, *288*(1–2), 320–328. https://doi.org/10.1016/j.epsl.2009.09.035

Lowry, A. R., & Pérez-Gussinyé, M. (2011). The role of crustal quartz in controlling Cordilleran deformation. *Nature*, *471*(7338), 353–357. https://doi.org/10.1038/nature09912

Luo, Y., Xu, Y., & Yang, Y. (2013). Crustal radial anisotropy beneath the Dabie orogenic belt from ambient noise tomography. *Geophysical Journal International*, *195*(2), 1149–1164. https://doi.org/10.1093/gji/ggt281

Mainprice, D., & Nicolas, A. (1989). Development of shape and lattice preferred orientations: Application to the seismic anisotropy of the lower crust. *Journal of Structural Geology*, *11*(1–2), 175–189. https://doi.org/10.1016/0191-8141(89)90042-4

Malory, A. O., Bao, X., & Chen, Z. (2022). Crustal shear wave velocity and radial anisotropy beneath Southern Africa from ambient noise tomography. *Tectonophysics*, *822*, 229191. https://doi.org/10.1016/j.tecto.2021.229191

Metcalfe, I. (2013). Gondwana dispersion and Asian accretion: Tectonic and palaeogeographic evolution of eastern Tethys. *Journal of Asian Earth Sciences*, *66*, 1–33. https://doi.org/10.1016/j.jseaes.2012.12.020

Moschetti, M. P., Ritzwoller, M. H., Lin, F., & Yang, Y. (2010). Seismic evidence for widespread western-US deep-crustal deformation caused by extension. *Nature*, *464*(7290), 885–889. https://doi.org/10.1038/nature08951

Panning, M., & Romanowicz, B. (2006). A three-dimensional radially anisotropic model of shear velocity in the whole mantle. *Geophysical Journal International*, *167*(1), 361–379. https://doi.org/10.1111/j.1365-246x.2006.03100.x

Park, J., & Levin, V. (2002). Seismic anisotropy: Tracing plate dynamics in the mantle. *Science*, *296*(5567), 485–489. https://doi.org/10.1126/science.1067319

Percival, J., Sanborn-Barrie, M., Skulski, T., Stott, G., Helmstaedt, H., & White, D. (2006). Tectonic evolution of the western Superior province from NATMAP and Lithoprobe studies. *Canadian Journal of Earth Sciences*, *43*(7), 1085–1117. https://doi.org/10.1139/e06-062

Rawlinson, N., & Sambridge, M. (2005). The fast marching method: An effective tool for tomographic imaging and tracking multiple phases in complex layered media. *Exploration Geophysics*, *36*(4), 341–350. https://doi.org/10.1071/eg05341

Schimmel, M., Stutzmann, E., & Gallart, J. (2011). Using instantaneous phase coherence for signal extraction from ambient noise data at a local to a global scale. *Geophysical Journal International*, *184*(1), 494–506. https://doi.org/10.1111/j.1365-246x.2010.04861.x

Shapiro, N. M., Ritzwoller, M. H., Molnar, P., & Levin, V. (2004). Thinning and flow of Tibetan crust constrained by seismic anisotropy. *Science*, *305*(5681), 233–236. https://doi.org/10.1126/science.1098276

Silver, P. G. (1996). Seismic anisotropy beneath the continents: Probing the depths of geology. *Annual Review of Earth and Planetary Sciences*, *24*(1), 385–432. https://doi.org/10.1146/annurev.earth.24.1.385

Sleep, N. H. (1990). Monteregian hotspot track: A long-lived mantle plume. *Journal of Geophysical Research*, *95*(B13), 21983–21990. https://doi.org/10.1029/jb095ib13p21983

Stachnik, J., Dueker, K., Schutt, D. L., & Yuan, H. (2008). Imaging Yellowstone plume-lithosphere interactions from inversion of ballistic and diffusive Rayleigh wave dispersion and crustal thickness data. *Geochemistry, Geophysics, Geosystems*, *9*(6). https://doi.org/10.1029/2008gc001992

Thybo, H., & Artemieva, I. (2013). Moho and magmatic underplating in continental lithosphere. *Tectonophysics*, *609*, 605–619. https://doi.org/10.1016/j.tecto.2013.05.032

Wan, B., Wu, F., Chen, L., Zhao, L., Liang, X., Xiao, W., & Zhu, R. (2019). Cyclical one-way continental rupture-drift in the Tethyan evolution: Subduction-driven plate tectonics. *Science China Earth Sciences*, *62*(12), 2005–2016. https://doi.org/10.1007/s11430-019-9393-4

Wang, D., & Shu, L. (2012). Late Mesozoic basin and range tectonics and related magmatism in Southeast China. *Geoscience Frontiers*, *3*(2), 109–124. https://doi.org/10.1016/j.gsf.2011.11.007

Wang, M., Hubbard, J., Plesch, A., Shaw, J. H., & Wang, L. (2016). Three-dimensional seismic velocity structure in the Sichuan basin, China. *Journal of Geophysical Research: Solid Earth*, *121*(2), 1007–1022. https://doi.org/10.1002/2015jb012644

Wang, M., & Shen, Z. K. (2020). Present-day crustal deformation of continental China derived from GPS and its tectonic implications. *Journal of Geophysical Research: Solid Earth*, *125*(2), e2019JB018774. https://doi.org/10.1029/2019jb018774

Wang, Y., Fan, W., Guo, F., Peng, T., & Li, C. (2003). Geochemistry of Mesozoic mafic rocks adjacent to the Chenzhou-Linwu fault, south China: Implications for the lithospheric boundary between the Yangtze and Cathaysia blocks. *International Geology Review*, *45*(3), 263–286. https://doi.org/10.2747/0020-6814.45.3.263

Wang, Y., Fan, W., Zhang, G., & Zhang, Y. (2013). Phanerozoic tectonics of the South China block: Key observations and controversies. *Gondwana Research*, *23*(4), 1273–1305. https://doi.org/10.1016/j.gr.2012.02.019

Wang, Y., Zhang, Y., Fan, W., Geng, H., Zou, H., & Bi, X. (2014). Early Neoproterozoic accretionary assemblage in the Cathaysia Block: Geochronological, Lu–Hf isotopic and geochemical evidence from granitoid gneisses. *Precambrian Research*, *249*, 144–161. https://doi.org/10.1016/j.precamres.2014.05.003

Wei, Z., Chen, L., Li, Z., Ling, Y., & Li, J. (2016). Regional variation in Moho depth and Poisson's ratio beneath eastern China and its tectonic implications. *Journal of Asian Earth Sciences*, *115*, 308–320. https://doi.org/10.1016/j.jseaes.2015.10.010

Weiss, T., Siegesmund, S., Rabbel, W., Bohlen, T., & Pohl, M. (1999). Seismic velocities and anisotropy of the lower continental crust: A review. *Seismic exploration of the deep continental crust: Methods and concepts of DEKORP and accompanying projects*, 97–122. https://doi.org/10.1007/978-3-0348-8670-3_6

Xie, J., Ritzwoller, M. H., Shen, W., & Wang, W. (2017). Crustal anisotropy across eastern Tibet and surroundings modeled as a depth-dependent tilted hexagonally symmetric medium. *Geophysical Journal International*, *209*(1), 466–491. https://doi.org/10.1093/gji/ggx004

Xie, J., Ritzwoller, M. H., Shen, W., Yang, Y., Zheng, Y., & Zhou, L. (2013). Crustal radial anisotropy across eastern Tibet and the western Yangtze craton. *Journal of Geophysical Research: Solid Earth*, *118*(8), 4226–4252. https://doi.org/10.1002/jgrb.50296

Xu, Z.-h. (2001). A present-day tectonic stress map for eastern Asia region. *Acta Seismologica Sinica*, *14*(5), 524–533. https://doi.org/10.1007/bf02718059

Yan, D.-P., Zhou, M.-F., Song, H.-L., Wang, X.-W., & Malpas, J. (2003). Origin and tectonic significance of a Mesozoic multi-layer over-thrust system within the Yangtze block (south China). *Tectonophysics*, *361*(3–4), 239–254. https://doi.org/10.1016/s0040-1951(02)00646-7

Yang, J. H., Zhang, J. H., Chen, J. Y., & Sun, J. F. (2021). Mesozoic continental crustal rejuvenation of South China: Insights from zircon Hf-O isotopes of early Jurassic gabbros, syenites and A-type granite. *Lithos*, 402–403.

Yao, W.-H., Li, Z.-X., Li, W.-X., Wang, X.-C., Li, X.-H., & Yang, J.-H. (2012). Post-kinematic lithospheric delamination of the Wuyi–Yunkai orogen in south China: Evidence from ca. 435 Ma high-Mg basalts. *Lithos*, *154*, 115–129. https://doi.org/10.1016/j.lithos.2012.06.033

Yuan, H., & Bodin, T. (2018). A probabilistic shear wave velocity model of the crust in the central West Australian Craton constrained by transdimensional inversion of ambient noise dispersion. *Tectonics*, *37*(7), 1994–2012. https://doi.org/10.1029/2017tc004834

Yuan, H., & Dueker, K. (2005). Upper mantle tomographic Vp and vs images of the Rocky Mountains in Wyoming, Colorado and New Mexico: Evidence for thick, laterally heterogeneous lithosphere. In G. Randy & K. E. Karlstrom (Eds.), *The Rocky mountain region--an evolving lithosphere: Tectonics, geochemistry, and geophysics* (pp. 329–345). American Geophysical Union.

Yuan, H., Dueker, K., & Stachnik, J. (2010). Crustal structure and thickness along the Yellowstone hot spot track: Evidence for lower crustal outflow from beneath the eastern Snake River Plain. *Geochemistry, Geophysics, Geosystems*, *11*(3). https://doi.org/10.1029/2009gc002787

Yuan, H., Zhao, L., Jiang, M., & Li, T. (2023). Datasets for "Continental fragments in the South China Block – Constraints from crustal radial anisotropy. *figshare. Dataset*. https://doi.org/10.6084/m9.figshare.22698181.v3

Zhang, G., Guo, A., Wang, Y., Li, S., Dong, Y., Liu, S., et al. (2013). Tectonics of South China continent and its implications. *Science China Earth Sciences*, *56*(11), 1804–1828. https://doi.org/10.1007/s11430-013-4679-1

Zhang, H., Lü, Q.-T., Wang, X.-L., Han, S., Liu, L., Gao, L., et al. (2023). Seismically imaged lithospheric delamination and its controls on the Mesozoic magmatic province in south China. *Nature Communications*, *14*(1), 2718. https://doi.org/10.1038/s41467-023-37855-5

Zhang, K., Lü, Q., Zhao, J., Yan, J., Hu, H., Luo, F., et al. (2020). Magnetotelluric evidence for the multi-microcontinental composition of eastern South China and its tectonic evolution. *Scientific Reports*, *10*(1), 13105. https://doi.org/10.1038/s41598-020-69777-3

Zhang, L., Jin, S., Wei, W., Ye, G., Jing, J., Dong, H., & Xie, C. (2015). Lithospheric electrical structure of South China imaged by magnetotelluric data and its tectonic implications. *Journal of Asian Earth Sciences*, *98*, 178–187. https://doi.org/10.1016/j.jseaes.2014.10.034

Zhang, Y., Chen, L., Ai, Y., Jiang, M., Xu, W., & Shen, Z. (2018). Lithospheric structure of the South China block from S-receiver function. *Chinese Journal of Geophysics*, *61*(1), 138–149.

Zhao, G., & Cawood, P. A. (2012). Precambrian geology of China. *Precambrian Research*, *222–223*, 13–54. https://doi.org/10.1016/j.precamres.2012.09.017

Zhou, L., Xie, J., Shen, W., Zheng, Y., Yang, Y., Shi, H., & Ritzwoller, M. H. (2012). The structure of the crust and uppermost mantle beneath South China from ambient noise and earthquake tomography. *Geophysical Journal International*, *189*(3), 1565–1583. https://doi.org/10.1111/j.1365-246X.2012.05423.x

Zhou, M.-F., Yan, D.-P., Kennedy, A. K., Li, Y., & Ding, J. (2002). SHRIMP U–Pb zircon geochronological and geochemical evidence for Neoproterozoic arc-magmatism along the western margin of the Yangtze Block, South China. *Earth and Planetary Science Letters*, *196*(1–2), 51–67. https://doi.org/10.1016/s0012-821x(01)00595-7

References From the Supporting Information

Bodin, T., Sambridge, M., Rawlinson, N., & Arroucau, P. (2012). Transdimensional tomography with unknown data noise. *Geophysical Journal International*, *189*(3), 1536–1556. https://doi.org/10.1111/j.1365-246X.2012.05414.x

Mooney, W. (2010). Crust and lithospheric structure-Global crustal structure. *Treatise on Geophysics*, *1*. https://doi.org/10.1016/B978-0-444-53802-4.00010-5

Xin, H., Zhang, H., Kang, M., He, R., Gao, L., & Gao, J. (2018). High-resolution lithospheric velocity structure of continental China by double-difference seismic travel-time tomography. *Seismological Research Letters*, *90*(1), 229–241. https://doi.org/10.1785/0220180209